

## RESEARCH LETTER

10.1002/2015GL063733

## Key Points:

- Interpolation of receiver function simplifies the complexity in the waveform
- Interpolated receiver functions are suitable for 3-D joint inversion study
- Jointly inverted velocity structures correlate with known tectonic provinces

## Supporting Information:

- Texts S1–S3, Figures S1–S16, Tables S1 and S2, Data Sets S1 and S2, Movie S1, and Software S1–S3
- Software S1
- Software S2
- Software S3
- Movie S1
- Figure S2
- Figure S3
- Figure S4
- Figure S8

## Correspondence to:

C. Chai,  
cchai@psu.edu

## Citation:

Chai, C., C. J. Ammon, M. Maceira, and R. B. Herrmann (2015), Inverting interpolated receiver functions with surface wave dispersion and gravity: Application to the western U.S. and adjacent Canada and Mexico, *Geophys. Res. Lett.*, 42, 4359–4366, doi:10.1002/2015GL063733.

Received 9 MAR 2015

Accepted 14 MAY 2015

Accepted article online 20 MAY 2015

Published online 9 JUN 2015

# Inverting interpolated receiver functions with surface wave dispersion and gravity: Application to the western U.S. and adjacent Canada and Mexico

Chengping Chai<sup>1</sup>, Charles J. Ammon<sup>1</sup>, Monica Maceira<sup>2</sup>, and Robert B. Herrmann<sup>3</sup>
<sup>1</sup>Department of Geosciences, Pennsylvania State University, University Park, Pennsylvania, USA, <sup>2</sup>Los Alamos National Laboratory, Los Alamos, New Mexico, USA, <sup>3</sup>Department of Earth and Atmospheric Sciences, Saint Louis University, St. Louis, Missouri, USA

**Abstract** We use *P* wave receiver functions from the western U.S. and adjacent regions to construct a receiver function wavefield interpolation scheme that helps to equalize the lateral sampling of the receiver functions and the surface wave dispersion and to greatly simplify the receiver functions. Spatial interpolation and smoothing suppress poorly sampled and difficult to interpret back azimuthal variations and allow the extraction of the first-order features in the receiver function wavefield, including observations from several ray parameter ranges. We combine the interpolated receiver functions with Rayleigh wave dispersion estimates and surface gravity observations to estimate the 3-D shear wave speed beneath the region. Speed variations in the 3-D model correlate strongly with expected geologic variations and illuminate broad-scale features of the western U.S. crust and upper mantle. The model is smooth, self-consistent, and demonstrates the compatibility of the interpolated receiver functions and dispersion observations.

## 1. Introduction

A simultaneous inversion of multiple, consistent, and complementary data sets is an ideal way to image the Earth's interior. Constraints from complementary data are generally easy to merge, and the result is more robust. These ideas have been illustrated by investigators who have produced estimates of the lithospheric structure by combining *P* wave receiver functions (RFs) and surface wave dispersion [e.g., Özalaybey *et al.*, 1997; Julià *et al.*, 2000, 2003, 2005; Shen *et al.*, 2013a, 2013b]. For large data sets, combining data can require a laborious examination of the RFs or sophisticated stacking approaches that may or may not be effective, depending on the ray parameter and azimuthal coverage in the receiver function collection. RF signals are often variable, and at times it is difficult to be sure that an underlying simple component of the signal exists. Small additions to a simple crust-mantle-transition-dominated RF can introduce vertical structural complexity that is as intriguing as it is difficult to validate. This is especially true for broader-band RFs, where short-period variation with incidence angle and azimuth can be dramatic. A second issue that has been difficult to address is the difference in spatial sampling of the receiver function and surface wave data. Surface waves produce broad, low wave number constraints on lateral variations in the structure, but RFs are sensitive to the higher wave number features of the structure. Though the combination for vertical resolution is ideal, the sensitivity difference is not ideal when we look at how each signal averages the lateral structure [Julià *et al.*, 2000]. Intermediate- and long-period surface waves laterally average heterogeneity (particularly when they are from smoothed tomographic inversions); RFs are relatively localized observations [Langston, 1979; Ammon *et al.*, 1990; Ammon, 1991]. This can create an incompatible pair of observations.

To explore these issues, we examined observations from the Transportable Array (TA), an ideal laboratory to explore the potential of seismic methods to image the subsurface by providing a more or less uniform sampling of the structure and the seismic wavefield. TA *P* wave RFs from western U.S. are used to construct a receiver function wavefield interpolation scheme that helps to equalize the lateral sensitivity of the RFs and the surface wave dispersion and that greatly simplifies the complexity in the RFs. Poorly sampled, difficult to interpret back azimuthal variations are suppressed, and receiver function estimates from several ray parameter ranges, which provide additional information on the seismic structure beneath the station, are stabilized. We sacrifice spatial resolution for a more self-consistent, smoother model, which has great value as a starting point for more detailed analyses of uninterpolated RFs to extract information on sharper geologic boundaries,

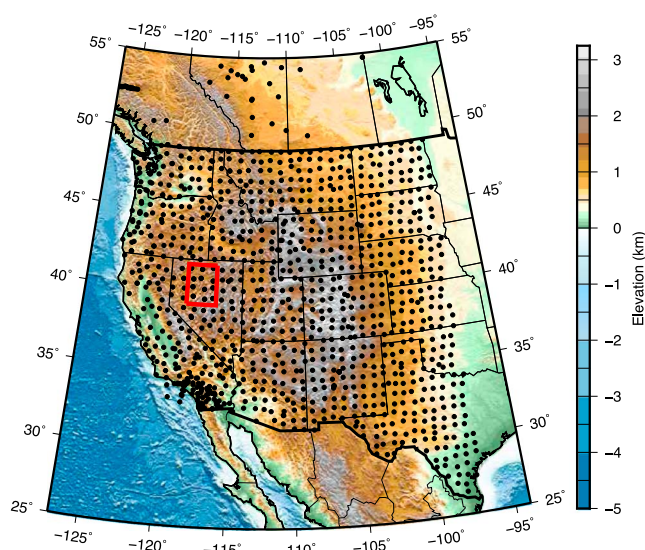


**Figure 1.** Map of the study region and the station locations (black dots) used in the receiver function wavefield interpolation. Stations in the red box identifies stations explored in Figure 3.

anisotropy, etc. The teleseismic  $P$  wavefield can be directly interpolated [e.g., *Poppeliers and Pavlis, 2003*], but the interpolation of RFs is easier to process. Interpolated RFs may result in simpler velocity models compared with other methods. Our model is generally consistent with published structural images based on multiple (but not identical) data sets.

## 2. The Receiver Function Wavefield of Western North America

Figure 1 is a map of the stations employed in our analysis. We used all the TA stations for which stable receiver function estimates [Ammon, 2013] were possible and included several other networks (see Table S1 in the supporting information). Using events with recorded magnitude  $m_b > 5.7$  (during station operation times) at epicentral distances from 30 to 100°, RFs were calculated at 1093 stations using the time domain iterative deconvolution algorithm [Ligorria and Ammon, 1999], with a Gaussian filter of 1.0 and 2.5 (corresponding to pulse widths of 1.67 and 0.67 s at half the maximum, respectively). We excluded RFs that originated from seismograms with signal-to-noise ratios (measured using the  $P$  wave signals) less than 10 and that corresponded to convolutional misfits less than 85% of the radial component signal power. In a traditional approach, we would stack RFs at each station and perform an inversion for the subsurface shear wave speed variations. Instead, the RF information was simplified by spatially interpolating and smoothing the  $P$  wave receiver function wavefield. Although interpolation is a natural consideration for simplifying observations, motivation to interpolate the wavefield comes from a holistic examination of the  $P$  wave RF response, which shows broad regions of correlation in the signals (Figure 2 and Movie S1). Superimposed on the spatially broad variations are smaller wave number (often single-station), large-amplitude fluctuations that complicate the analysis of the first-order features in the receiver function response (Figure 2). The deeper mantle conversions in the RFs are also simplified by interpolation. Though our focus is the shallow responses (−5 to 40 s), the interpolation works for deeper signals.

## 3. Receiver Function Interpolation and Smoothing

Our interpolation approach is straightforward, produced by sample-by-sample interpolation of the observed wavefield. Consider a particular location of interest (LOI) within the study region. For each nearby station, all available receiver function measurements are binned into three ray parameter ranges, corresponding to values larger than 0.07 s/km, between 0.05 and 0.07 s/km, and smaller than 0.05 s/km, respectively. Station binning equalizes the importance of the nearby stations, accounting for differences in the number of observations at each station. Long-deployed stations produce thousands of useable RFs, but the observations at a majority of TA stations produce dozens due to the limited operation period. For each ray parameter range, the RF at the LOI is computed from a weighted average of all the station-centered waveforms within a specific

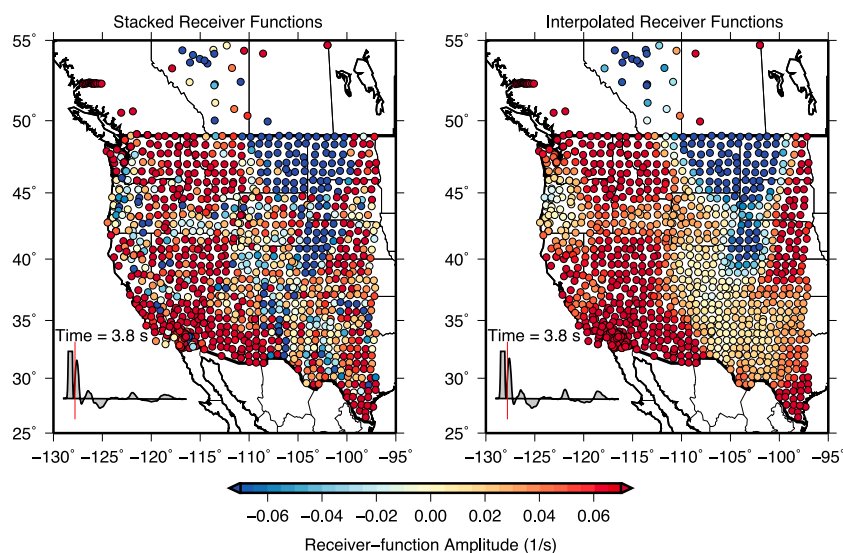


**Figure 2.** Time slices at time 3.8 s from the receiver function wavefield in the western U.S. and adjacent Canada. Each circle represents a seismic station at which we have computed a stacked RF. The color indicates the amplitude of (left) the receiver function stacked at each station or (right) the interpolated value of the receiver function wavefield. Inset shows the stack of all RFs, and the red line shows the location of the time slice, which was chosen to show the structure near the time of the  $P_s$  converted phase arrival from the crust-mantle transition region. The interpolation parameters  $d_1$  of 150 km and  $d_2$  of 250 km were used in Figure 2 (right).

distance,  $d_2$ , from the LOI. Each RF is weighted to give more importance to stations closest to the LOI. Weight for signals recorded within a distance  $d_1$  was 1.0, while those located between the distance  $d_1$  and the distance  $d_2$  of the LOI decreased linearly from 1.0 to 0.0 across the range from  $d_1$  to  $d_2$ . An interpolated RF was computed by summing the weighted, binned RFs and normalized by the sum of the weights. The distance ranges can be chosen considering the station spacing and the amount of smoothing desired. For the TA ( $\sim 70$  km station spacing),  $d_2$  was set to 250 km so that normally 30–52 stations are used to interpolate and smooth each RF. These distances were selected empirically to match the spatial coherence observable in the unsmoothed receiver function wavefield. Usually, 8–24 stations are located within the distance of  $d_1$ , 150 km. If a  $d_2$  of 110 km ( $d_1$  of 80 km) is chosen, typically 6–11 stations are used to generate a RF producing a wavefield that includes more power in the higher wave numbers, which is often due to shallow, localized structure. An interpolated RF is generally calculated from thousands of waveforms compared to dozens for the simple stack at a normal TA station, which increases the signal-to-noise ratio significantly (suppressing spatially incoherent components of the signal) and allows us to construct RFs in three ray parameter ranges.

A time slice of the interpolated response for the intermediate ray parameter range is shown in Figure 2. As expected, interpolation produces a broad average of the RF response, smoothing over sporadic fluctuations in the wavefield, and smoothing across sharp boundaries in the ground deformation. Variation in the wavefield complexity changes directly with the chosen values of smoothness control parameters ( $d_1$  and  $d_2$ ). Interpolation and smoothing can be adjusted to enhance the well-resolved low wave number components of the receiver function wavefield (Figure 2). The spatially correlated anomalies in the interpolated receiver function wavefield are comparable to those in the surface wave observations from ambient noise tomography [Herrmann *et al.*, 2013]. Synthetic tests and 1-D inversion results show receiver function interpolation suppressed noise and potential scattering artifacts (see Text S1 and Figures S11–S14). The value of the interpolation parameters shows the lateral extent of anomalies that can be extracted. Ideally, we should start the analysis of the RFs using large interpolation parameters and gradually decrease the interpolation parameters. Although we apply the method to a large network, in Text S2 and Figures S15 and S16 we show how this approach can extract average responses from smaller networks with adjustments to  $d_1$  and  $d_2$ . We expect our method to be successfully applied to existing and future network data. The interpolation distances should be based on station spacing and assumed scale of heterogeneity.

The effectiveness of the interpolation scheme is illustrated using 12 RFs from north central Nevada (stations in the box in Figure 1). Stacked and interpolated RFs for stations M08A–M10A, N08A–N10A, O08A–O10A, and

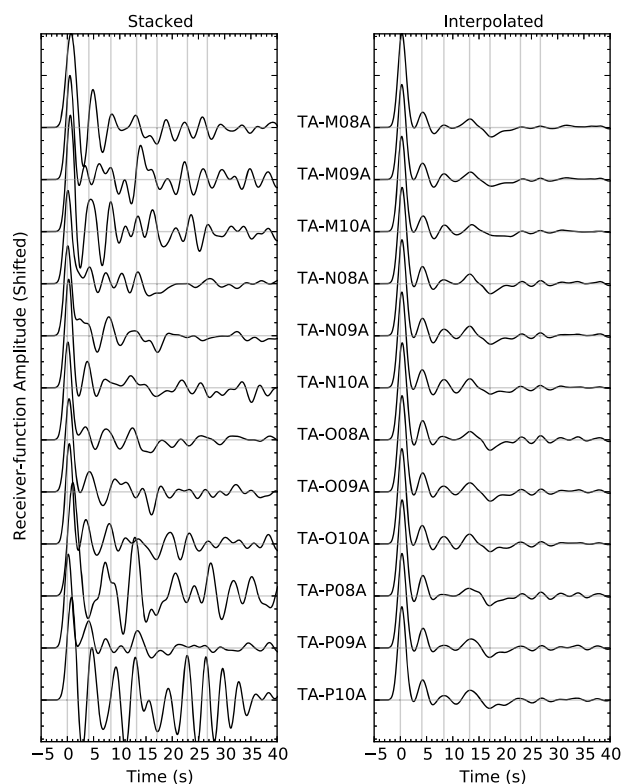


**Figure 3.** Stacked and interpolated RFs for TA stations M08A-M10A, N08A-N10A, O08A-O10A, and P08A-P10A from central Nevada (see red box in Figure 1 for station locations). The interpolated RFs were computed with the binned RFs within 250 km distance of the station using weights according to the distance from each station. Midrange ray parameter bins with Gaussian 1.0 are shown for the interpolated RFs. The simple stack uses all RFs with Gaussian 1.0. The amplitude scale is the same for all waveforms.

measurements at any location within the densely sampled region of stations (similar to an independent study [Zhang and Zheng, 2015]). To simplify the 3-D shear wave speed inversion, the wavefield was interpolated to an evenly sampled grid with  $1^\circ$  spacing.

#### 4. Inversion for 3-D Shear Wave Speed Variations

To estimate the subsurface shear wave speeds beneath the study region and demonstrate the compatibility of the interpolated RFs with other data, we inverted the interpolated receiver function wavefield, Rayleigh wave group velocities in the period range from 7 to 250 s, and wave number-filtered Bouguer gravity observations (see Acknowledgements). RFs windowed between  $-5$  and 40 s for Gaussian 1.0 and between  $-5$  and 10 s for Gaussian 2.5 (in the region of the TA) were used to constrain the resulting model. The study region was divided into  $900\ 1^\circ$  by  $1^\circ$  size cells, and a one-dimensional, isotropic shear wave speed model was estimated for each cell. A linearized discrete geophysical inversion was used with smoothness-based stabilization (developed from Maceira and Ammon [2009] and Julià et al. [2000]). We included vertical smoothness constraints that increase with depth and require that the model approach an a priori model (see Acknowledgements). A Laplacian-based lateral smoothing that does not smooth across the ocean-continent boundary is used to allow a sharp change in material properties across this well-defined feature. Partial derivatives for the RFs [Randall, 1994] and surface waves were computed using finite-difference approximations, and the gravity derivatives were computed using the equations from Plouff [1976]. The  $V_p/V_s$  ratio was fixed throughout the inversion (inherited from the initial model).

To avoid mapping broad, possibly dynamically caused features in the western U.S. gravity field into density and shear wave speed variations, we high pass wave number filter the surface gravity measurements with

P08A-P10A are shown in Figure 3. The interpolated RFs were computed by combining RFs within 250 km distance of the station using weights described above. The simple stacks show dramatic variations across the region that we suspect is most likely associated with near-surface variations in this small section of the Basin and Range (BR) Province. The smoothing effect is obvious for TA stations P10A and P08A, but even the smaller-amplitude signals on the other waveforms are simplified by interpolation. Where the stacks are simple, they are similar to the interpolated RFs, providing confidence that the interpolation worked to extract the common, deeper structural features in the RFs. The net result is an enhancement of arrivals most likely associated with the crust-mantle transition and other first-order features (velocity contrasts) in the crust and uppermost mantle. The change in signal amplitudes is relatively small for these Gaussian 1.0 observations. Interpolation can have a stronger effect on the amplitude of the broadband (Gaussian 2.5) converted phases and multiples that vertically smooths the resulting shear wave velocity model. Finally, the RF interpolation allows us to estimate receiver function measure-



a simple boxcar filter with a width of four cells ( $\sim 440$  km). We use the density-shear velocity relationship employed by *Maceira and Ammon* [2009], which integrates an empirical relation appropriate for sedimentary rocks [*Nafe and Drake*, 1961] with a linear relationship from *Birch* [1961] that is more applicable to denser rocks. The relationship may need adjustment to extract details in the shallowest regions of sedimentary basins, but the results are reliable to first order. Gravity constraints are only included in the central part of the model since we include a four-cell boundary to avoid edge effects in the gravity calculations (Figure S5). Inversions with and without gravity were performed to test the sensitivity of the results to the gravity data. For the most part, gravity induces only slight changes (0.05 km/s or less) in the near-surface shear wave speeds. The region of greatest shear velocity change (roughly 0.1 km/s) is located just off the coast of California, in the area where the gravity change is maximal and both the data and smoothness constraints are minimal. Where available (generally within the TA region), we included six RFs for each cell, including two Gaussian width parameters (1.0 and 2.5) and the three ray parameter ranges described previously.

The inversion started from the initial model (Data Set S1). Since flat-Earth codes were used to compute dispersion, the initial model was flattened using the formulas from *Biswas* [1972] with a slightly modified density transformation exponent (2.275 (D. Harkrider, personal communication, 2004); Text S3). The inverted model was unflattened accordingly for interpretation and easy comparison with other published spherical-Earth models. In areas that contain relatively simple structures, the inversion of both data is relatively simple; however, our experience suggested that the RF inversions in regions of large near-surface low-velocity regions (e.g., the Gulf Coast Basin, GCB, and the Williston and Denver Basins, WDB) converged more easily to geologically reasonable models after an initial fit to only the dispersion. So our initial inversion omitted RFs from the regions of thick and dramatic sedimentary structure (e.g., the GCB and the WDB). This approach allowed the dispersion observations to adjust the initial model into the correct region of model space after which an inversion that included all the data in each cell was followed.

The inversions included two sets of four-iteration inversions (the second set is for gravity observations and the stepwise inversion of regions with thick sedimentary basins describe above). The final model (Data Set S2) is selected according to the misfit from over 200 sets of inversions using different inversion parameters. In each inversion the convergence was rapid for the first iteration and then more gradual. Variance reduction values for the RF, dispersion, and gravity were roughly 55%, 81%, and 93%. The reductions are of course dependent on the reference model. About 98% of the dispersion misfits are within 0.2 km/s, improved from 7% for the initial model, and 92% of the receiver function misfits are within 60% of the signal power, comparing to 11% of the initial misfits. An inversion with only dispersion and gravity observations produced variance reductions of 80% and 94%, respectively, adding the RFs little affects the fit to the other data (the same is true for stacked RFs). The numbers help summarize the fits, but we also examined each RF and dispersion curve fit visually, and the fit improvement is significant (Figures S2–S4). All the fits were generally good, although some systematic variations are notable. Predicted short-period RFs in regions of thick sedimentary sequences contained more detail (different from unsmoothed RFs) than is visible in the data, which we attribute to not accounting for attenuation or lateral structure in the near surface. Fitting signals near the Gulf Coast was problematic with simple 1-D velocity structures. We leave exploration and exploitation of these details for more geographically focused future efforts. The variance reduction in a similar inversion with stacked RFs was 51%, and the fits were noticeably (visibly) poorer. We do not provide a detailed analysis of uncertainty, which is much more difficult to estimate given the integration of tomography observations from several studies, gravity observations, RF smoothing, and theoretical assumptions used in the modeling. Our experience based on multiple inversions and forward modeling suggests that the general trends are reasonably resolved and that the speeds are likely within 0.1–0.2 km/s of the true values (accounting for the spatial averaging performed by the data and modeling assumptions). In the basins, the need for assumed velocity-density and  $V_p/V_s$  ratios increases the velocity uncertainty. Since our focus is on the benefits of RF spatial interpolation, we leave these important assessments for the future, but note that we have confidence in the first-order variations in the subsurface reconstruction.

## 5. Discussion

The inversion results are summarized with depth slices in Figures S7 and S8 and shown in a summary profile format in Figure 4. After many decades of effort, much is known about the subsurface beneath the active tectonic region of North America and the transition to the Great Plains. Examination of Figure S7 demonstrates that to first order, our model is consistent with those of other researchers [e.g., *Bedle and van der Lee*, 2009;

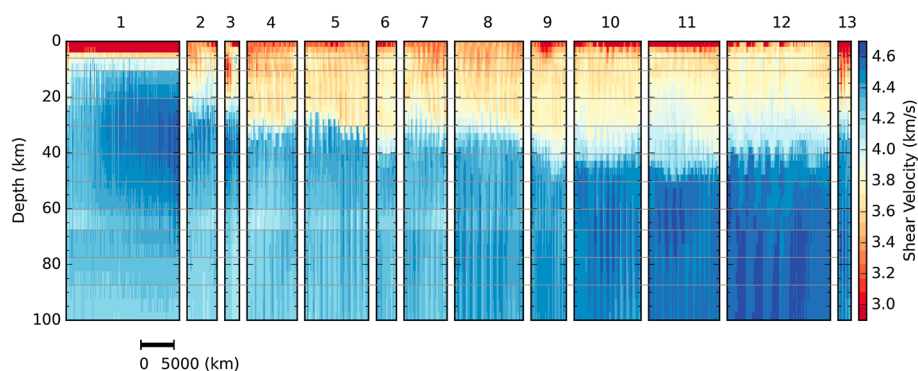


**Figure 4.** Earth model clusters constructed using a Euclidean distance metric. The clusters correspond well to the known geomorphic/geologic provinces in the western United States. Westernmost regions are shown on the left, regions from the interior of North America toward the right, and oceanic regions are on the first left (sorted by ocean age). Velocity profiles within the cluster are sorted from north to south by row (like lines in a book). The large cell size prohibits resolution of small provinces, but the rough correspondence of the clusters to geologic regions are (1) oceanic, (2) Gulf of California region, (3) NW Pacific Coast Range System, (4) Northern Basin and Range, (5) southern BR region, (6) Colorado Plateaus, (7) Columbia River Plateau region, (8) Northern Rocky Mountains, (9) Middle and Southern Rocky Mountains, (10) Great Plains, (11) Williston and Denver Basins, (12) Canadian Craton, and (13) Gulf Coast Basin. The spatial distribution of the clusters is shown in Figure S9. The dendrogram is included in Figure S10.

Obrebski *et al.*, 2011; Porritt *et al.*, 2014; Shen *et al.*, 2013a; Burdick *et al.*, 2014]. The basins are nicely imaged, and the main crustal features are visible. Structures nearest the surface rely on more sparse observations which requires the need to smooth at the shortest periods. The well-known first-order variations in the uppermost mantle are apparent (controlled directly by the long-period dispersion and only indirectly by the RFs, which primarily sharpen the crustal structure). The interior of North America is fast, the western tectonic regions slow. More subtle regional variations become apparent with a more detailed analysis of the velocity structures. In particular, low shear wave speeds are seen in the midcrust under the BR, as well as beneath northern coastal California, northern Idaho, Oregon, and the Rio Grande rift. In the middle to lower crust, we see low velocities beneath the Aspen Anomaly [Ducker *et al.*, 2001], the San Francisco Peaks, the Cascade Range, and the northwestern BR. Near Moho depths of 38–40 km we see low velocities beneath the Rocky Mountains, Colorado Plateau (CP), and the Snake River Plain indicating thicker crust for those provinces. Low velocities beneath the Cascade Mountains likely reflect warm temperatures and/or crustal thickening. To the south of the CP, beneath the southern BR, we see higher than average velocities indicative of the thinner crust in that region. A broad upper mantle low-velocity region resides beneath northern Nevada in depth range from about 60 to 80 km.

An automated cluster analysis was used (based on Euclidean length, similar to Lekic and Romanowicz [2011]) to separate the 1-D shear velocity profiles into clusters of similar Earth structure. The clustered models are shown in Figure 4 (the corresponding spatial distribution of the clusters is shown in Figure S9). Small clusters and oceanic clusters were merged with nearby clusters to focus on first-order features. Profiles within a cluster are sorted from north to south by row and from west to east in a row. The clusters correlate strongly with known geomorphic/tectonic provinces with smoothing across the boundaries and blurring of some of the smaller provinces and transitions that are hard to resolve with  $1^\circ$  cells. The oceanic profiles are arranged by increasing ocean age which shows the expected difference between the Pacific and Juan de Fuca Plates, but our resolution of detailed structure in the oceans is severely limited, so we offer little interpretation.

The results are rich in detail, but many of the features in the western United States have been noted earlier, so we avoid specific, detailed discussions. But the consistency of the results with analyses from decades of research provides confidence in the 3-D structure as a robust model of the first-order variations in the crust and upper mantle structure beneath the region. Some general patterns include the suggestion that the lower crustal wave speeds in the northern BR are slightly lower than those of the southern BR, and the crustal thickness is less to the south. The upper mantle beneath the two regions is comparable, with the base of the lid roughly located at a depth of 60–70 km (agrees with Hopper *et al.* [2014] and Lekic and Fischer [2014]). The CP crust is thicker, with lithosphere more similar to regions to the west such as the Southern BR than the Rocky Mountains and Great Plains to the north and east, which suggests a modification of the mantle lid within the region [Levander *et al.*, 2011; Roy *et al.*, 2009]. The Columbia River Plateau has relatively low upper crustal

speeds, a typical lower crust, and an upper mantle that is faster to the region to the south but slower than that beneath stable North America to the east. Near-surface sedimentary structures are substantial beneath the WDB. Although our model for the bulk crust beneath the Williston Basins seems reasonable, the RFs include long reverberations (see Figure S2) that make seeing the deeper details difficult. Forward modeling of the signals does suggest that the area is not underlain by a sharp crust-mantle transition, which would create multiple arrivals in the RF that are not visible in the observations. As expected, the cratonic regions are underlain by uniformly fast mantle and have thin regions of relatively low speeds (sedimentary cover) near the surface.

## 6. Conclusions

The key idea presented in this paper is that using wavefield interpolation, we can simplify the receiver function wavefield to have a similar wave number sensitivity as seismic dispersion and gravity observations, which allows us to construct a reliable, smooth 3-D model of the subsurface. Waveform interpolation uses information from nearby stations to reduce scattering effects in single-station RFs and increases the sampling of the wavefield with incidence angle (ray parameter). Sacrificing resolution for consistency helps construct a model with a better balance in sensitivity to lateral heterogeneity, and it is likely to be a better starting place for more sophisticated fully 3-D inversions [e.g., *Tape et al.*, 2009; *Stich et al.*, 2009]. To some extent, the smoothness constraints of any practical inversion scheme must perform a similar smoothing procedure to produce a compromise fit to the different data sets, which would show in a simulation of the RFs using the inverted model. The resulting smoothed model provides a framework for more detailed work in regions of interest with reliable broadband constraints. The reduction of RFs provides opportunities for including these simple observations with more complete inversions including regional and perhaps teleseismic waveforms. The 3-D shear wave speed constructed with the interpolated wavefield strongly correlates with many ideas of western U.S. structure and represents a valuable starting point for more detailed regional and more fully 3-D seismic investigations.

## References

- Ammon, C. (2013), What can you learn from a million receiver functions?, Abstracts S24A-04 presented at 2013 Fall Meeting, AGU, San Francisco, Calif., 9–13 Dec.
- Ammon, C. J. (1991), The isolation of receiver effects from teleseismic *P* waveforms, *Bull. Seismol. Soc. Am.*, *81*(6), 2504–2510, doi:10.1029/JB095iB10p15303.
- Ammon, C. J., G. E. Randall, and G. Zandt (1990), On the nonuniqueness of receiver function inversions, *J. Geophys. Res.*, *95*(B10), 15,303–15,318, doi:10.1029/JB095iB10p15303.
- Balmino, G., N. Vales, S. Bonvalot, and A. Briaies (2012), Spherical harmonic modelling to ultra-high degree of Bouguer and isostatic anomalies, *J. Geod.*, *86*(7), 499–520, doi:10.1007/s00190-011-0533-4.
- Bede, H., and S. van der Lee (2009), *S* velocity variations beneath North America, *J. Geophys. Res.*, *114*, B07308, doi:10.1029/2008JB005949.
- Beyreuther, M., R. Barsch, L. Krischer, T. Megies, Y. Behr, and J. Wassermann (2010), ObsPy: A python toolbox for seismology, *Seismol. Res. Lett.*, *81*(3), 530–533, doi:10.1785/gssrl.81.3.530.
- Birch, F. (1961), The velocity of compressional waves in rocks to 10 kilobars: Part 2, *J. Geophys.*, *66*(7), 2199–2224, doi:10.1029/JZ066i007p02199.
- Biswas, N. N. (1972), Earth-flattening procedure for the propagation of Rayleigh wave, *Pure Appl. Geophys.*, *96*(1), 61–74, doi:10.1007/BF00875629.
- Burdick, S., R. D. van der Hilst, F. L. Vernon, V. Martynov, T. Cox, J. Eakins, G. H. Karasu, J. Tylell, L. Astiz, and G. L. Pavlis (2014), Model update January 2013: Upper mantle heterogeneity beneath North America from travel-time tomography with global and USArray transportable array data, *Seismol. Res. Lett.*, *85*(1), 77–81, doi:10.1785/0220130098.
- Christopher, A., and B. W. Eakins (2009), ETOPO1 1 arc-minute global relief model: Procedures, data sources and analysis, NOAA Tech. Memorandum NESDIS NGDC-24, Natl. Geophys. Data Center, NOAA, doi:10.7289/V5C8276M.
- Ducker, K., H. Yuan, and B. Zurek (2001), Thick-structured Proterozoic lithosphere of the Rocky Mountain region, *GSA Today*, *11*, 4–9.
- Ekström, G. (2011), A global model of Love and Rayleigh surface wave dispersion and anisotropy, 25–250 s, *Geophys. J. Int.*, *187*(3), 1668–1686, doi:10.1111/j.1365-246X.2011.05225.x.
- Herrmann, R. B. (2013), Computer programs in seismology: An evolving tool for instruction and research, *Seismol. Res. Lett.*, *84*(6), 1081–1088, doi:10.1785/0220110096.
- Herrmann, R. B., C. J. Ammon, and H. Benz (2013), Group velocity dispersion for North America. [Available at [http://www.eas.slu.edu/eqc/eqc\\_research/NATOMO](http://www.eas.slu.edu/eqc/eqc_research/NATOMO).]
- Hopper, E., H. A. Ford, K. M. Fischer, V. Lekic, and M. J. Fouch (2014), The lithosphere-boundary and the tectonic and magmatic history of the northwestern United States, *Earth Plane. Sci. Lett.*, *402*, 69–81, doi:10.1016/j.epsl.2013.12.016.
- Hunter, J. D. (2007), Matplotlib: A 2D graphics environment, *Comput. Sci. Eng.*, *9*(3), 90–95, doi:10.1109/MCSE.2007.55.
- Julià, J., C. J. Ammon, R. B. Herrmann, and A. M. Correig (2000), Joint inversion of receiver function and surface wave dispersion observations, *Geophys. J. Int.*, *143*(1), 99–112, doi:10.1046/j.1365-246x.2000.00217.x.
- Julià, J., C. J. Ammon, and R. B. Herrmann (2003), Lithospheric structure of the Arabian Shield from the joint inversion of receiver functions and surface-wave group velocities, *Tectonophysics*, *371*(1–4), 1–21, doi:10.1016/S0040-1951(03)00196-3.
- Julià, J., C. J. Ammon, and A. A. Nyblade (2005), Evidence for mafic lower crust in Tanzania, East Africa, from joint inversion of receiver functions and Rayleigh wave dispersion velocities, *Geophys. J. Int.*, *162*(2), 555–569, doi:10.1111/j.1365-246X.2005.02685.x.
- Kennett, B. L. N., E. R. Engdahl, and R. Buland (1995), Constraints on seismic velocities in the Earth from traveltimes, *Geophys. J. Int.*, *122*(1), 108–124, doi:10.1111/j.1365-246X.1995.tb03540.x.

## Acknowledgments

The facilities of the IRIS Data Services, and specifically the IRIS Data Management Center, were used for access to waveforms and related metadata required for receiver function data. IRIS Data Services are funded through the Seismological Facilities for the Advancement of Geoscience and EarthScope (SAGE) Proposal of the National Science Foundation under cooperative agreement EAR-1261681. The Rayleigh wave group velocities are a blend of observations from Herrmann *et al.*'s [2013] short-period observations and the intermediate- and long-period observations from Ekström [2011]. The data were blended across the period range from 25 to 80 s to cover a total period range from 7 to 250 s, adjusting cells with discrepancies individually. Gravity observations were obtained from Balmino *et al.* [2012]. The initial model (available in Data Set S1; Software S1 can convert the model to a format of Computer Programs in Seismology [Herrmann, 2013]; Software S2 and S3 can be used to interpolate 1-D profile) was based on Crust Model 1.0 [Laske *et al.*, 2013; REM, 2013]. Velocities at depth were initialized with the AK135 velocity model [Kennett *et al.*, 1995]. Elevation data used for Figure 1 were extracted from Christopher and Eakins [2009]. Ocean age date used for Figure 4 came from Müller *et al.* [2008]. We thank Martin Pratt, three anonymous reviewers, and Michael Wyssession (Editor) for their constructive criticism to greatly improve the manuscript. This work was supported by the U.S. DOE (grant LDRD-20120047ER) and by the U.S. National Science Foundation (grants EAR-1053484 and EAR-1053363). Thanks to developers of the Generic Mapping Tools (GMT) [Wessel *et al.*, 2013], ObsPy [Beyreuther *et al.*, 2010], Numpy [van der Walt *et al.*, 2011], and Matplotlib [Hunter, 2007]. We also thank Andrew Nyblade, Kevin Furlong, Sridhar Anandakrishnan, Erica Emry, and Matthew Herman for their discussions of the results.

The Editor thanks Martin Pratt and an anonymous reviewer for their assistance in evaluating this paper.

- Langston, C. A. (1979), Structure under Mount Rainier, Washington, inferred from teleseismic body waves, *J. Geophys. Res.*, *84*(B9), 4749–4762, doi:10.1029/JB084iB09p04749.
- Laske, G., G. Masters, Z. Ma, and M. Pasyanos (2013), Update on CRUST1.0—A 1-degree global model of Earth's crust, Abstracts EGU2013-2658 presented at 2013 EGU General Assembly Conference, Vienna, Austria, 7–12 April.
- Lekic, V., and K. M. Fischer (2014), Contrasting lithospheric signatures across the western United States revealed by Sp receiver functions, *Earth Planet. Sci. Lett.*, *402*, 90–98, doi:10.1016/j.epsl.2013.11.026.
- Lekic, V., and B. Romanowicz (2011), Tectonic regionalization without a priori information: A cluster analysis of upper mantle tomography, *Earth Planet. Sci. Lett.*, *308*(1–2), 151–160, doi:10.1016/j.epsl.2011.05.050.
- Levander, A., B. Schmandt, M. S. Miller, K. Liu, K. E. Karlstrom, R. S. Crow, C. T. A. Lee, and E. D. Humphreys (2011), Continuing Colorado Plateau uplift by delamination-style convective lithospheric downwelling, *Nature*, *472*(7344), 461–465, doi:10.1038/nature10001.
- Ligorria, J. P., and C. J. Ammon (1999), Iterative deconvolution and receiver-function estimation, *Bull. Seismol. Soc. Am.*, *89*(5), 1395–1400.
- Maceira, M., and C. J. Ammon (2009), Joint inversion of surface wave velocity and gravity observations and its application to central Asian basins shear velocity structure, *J. Geophys. Res.*, *114*, B02314, doi:10.1029/2007JB005157.
- Müller, R. D., M. Sdrolias, C. Gaina, and W. R. Roest (2008), Age, spreading rates, and spreading asymmetry of the world's ocean crust, *Geochim. Geophys. Geosyst.*, *9*, Q04006, doi:10.1029/2007GC001743.
- Nafe, J. E., and C. L. Drake (1961), Physical properties of marine sediments, *Tech. Rep., TR-2*, Lamont Geological Observatory, Palisades, New York.
- Obrebski, M., R. M. Allen, F. Pollitz, and S. H. Hung (2011), Lithosphere-aesthenosphere interaction beneath the western United States from the joint inversion of body-wave traveltimes and surface-wave phase velocities, *Geophys. J. Int.*, *185*(2), 1003–1021, doi:10.1111/j.1365-246X.2011.04990.x.
- Özalaybey, S., M. K. Savage, A. F. Sheehan, J. N. Louie, and J. N. Brune (1997), Shear-wave velocity structure in the northern Basin and Range Province from the combined analysis of receiver functions and surface waves, *Bull. Seismol. Soc. Am.*, *87*(1), 183–199.
- Plouff, D. (1976), Gravity and magnetic fields of polygonal prisms and application to magnetic terrain corrections, *Geophysics*, *41*(4), 727–741, doi:10.1190/1.1440645.
- Poppeliers, C., and G. L. Pavlis (2003), Three-dimensional, prestack, plane wave migration of teleseismic P-to-S converted phases: 1. Theory, *J. Geophys. Res.*, *108*(B2), 2112, doi:10.1029/2001JB000216.
- Porritt, R. W., R. M. Allen, and F. F. Pollitz (2014), Seismic imaging east of the Rocky Mountains with USArray, *Earth Planet. Sci. Lett.*, *402*, 16–25, doi:10.1016/j.epsl.2013.10.034.
- Randall, G. E. (1994), Efficient calculation of complete differential seismograms for laterally homogeneous Earth models, *Geophys. J. Int.*, *118*(1), 245–254, doi:10.1111/j.1365-246X.1994.tb04687.x.
- REM (2013), The Reference Earth Model. [Available at <http://igppweb.ucsd.edu/gabi/rem.html>.]
- Roy, M., T. H. Jordan, and J. Pederson (2009), Colorado Plateau magmatism and uplift by warming of heterogeneous lithosphere, *Nature*, *459*(7249), 978–982, doi:10.1038/nature08052.
- Shen, W., M. H. Ritzwoller, and V. Schulte Pelkum (2013a), A 3-D model of the crust and uppermost mantle beneath the central and western U.S. by joint inversion of receiver functions and surface wave dispersion, *J. Geophys. Res. Solid Earth*, *118*, 262–276, doi:10.1029/2012JB009602.
- Shen, W., M. H. Ritzwoller, V. Schulte Pelkum, and F.-C. Lin (2013b), Joint inversion of surface wave dispersion and receiver functions: A Bayesian Monte-Carlo approach, *Geophys. J. Int.*, *192*(2), 807–836, doi:10.1093/gji/ggs050.
- Stich, D., P. Danecek, A. Morelli, and J. Tromp (2009), Imaging lateral heterogeneity in the northern Apennines from time reversal of reflected surface waves, *Geophys. J. Int.*, *177*(2), 543–554, doi:10.1111/j.1365-246X.2008.04044.x.
- Tape, C., Q. Liu, A. Maggi, and J. Tromp (2009), Adjoint tomography of the Southern California crust, *Science*, *325*(5943), 988–992, doi:10.1126/science.1175298.
- van der Walt, S., S. C. Colbert, and G. Varoquaux (2011), The NumPy array: A structure for efficient numerical computation, *Comput. Sci. Eng.*, *13*(2), 22–30.
- Wessel, P., W. H. F. Smith, R. Scharroo, J. Luis, and F. Wobbe (2013), Generic Mapping Tools: Improved version released, *Eos Trans. AGU*, *94*(45), 409–410, doi:10.1002/2013EO450001.
- Zhang, J., and T. Zheng (2015), Receiver function imaging with reconstructed wavefields from sparsely scattered stations, *Seismol. Res. Lett.*, *86*(1), 165–172, doi:10.1785/0220140028.